Title

Energy Decomposition Analysis for Interactions of Radicals: Theory and Implementation at the MP2 Level with Application to Hydration of Halogenated Benzene Cations and Complexes between CO_2 –· and Pyridine and Imidazole

Journal

The Journal of Physical Chemistry A, 123(44)

ISSN

1089-5639

Authors

Loipersberger, Matthias
Lee, Joonho
Mao, Yuezhi
et al.

Publication Date

2019-11-07

DOI

10.1021/acs.jpca.9b08586

Peer reviewed

Energy Decomposition Analysis for Interactions of Radicals: Theory and Implementation at the MP2 Level with Application to Hydration of Halogenated Benzene Cations and Complexes between $CO_2^{-\bullet}$ and Pyridine and Imidazole

Matthias Loipersberger,[†] Joonho Lee,[†] Yuezhi Mao,[†] Akshaya K. Das,[†] Kevin Ikeda,[†] Jonathan Thirman,[†] Teresa Head-Gordon,[†,‡] and Martin Head-Gordon*[,†]

†*Department of Chemistry, University of California, Berkeley, CA 94720, USA*

‡*Department of Bioengineering, University of California, Berkeley, CA 94720, USA*

E-mail: mhg@cchem.berkeley.edu

Abstract

To study intermolecular interactions involving radicals at the correlated level, the Energy Decomposition Analysis scheme for Second-Order Møller-Plesset Perturbation Theory based on Absolutely Localized Molecular Orbitals (ALMO-MP2-EDA) is generalized to unrestricted and restricted open-shell MP2. The benefit of restricted open-shell MP2 is that it can provide accurate binding energies for radical complexes where density functional theory can be error prone due to delocalization errors. As a model application, the open-shell ALMO-MP2-EDA is applied to study the first solvation step of halogenated benzene radical cations, where both halogen and hydrogen bonded isomers are possible. We determine that the lighter halogens favor the hydrogen-bonded form, while the iodine-substituted species prefers halogen bonding due to larger polarizability and charge transfer at the halogen. As a second application, relevant to the activation of CO_2 in photoelectrocatalysis, complexes of $CO_2^{-\bullet}$ interacting with both pyridine and imidazole are analyzed with ALMO-MP2-EDA. The results reveal the importance of charge transfer into the π^* orbital of the heterocycle in controlling the stability of the carbamate binding mode, which is favored for pyridine, but not for imidazole.

1 Introduction

Intermolecular interactions describe attractive or repulsive forces between molecular species that govern important chemical processes, like the formation and structure of biological macromolecules and a wide range of catalyst systems.[1–10] Their energy scale ranges from a few kJ/mol for weak van der Waals complexes to more than 150 kJ/mol for strong hydrogen bonds or metal ligand interactions. The origin of these interactions can be understood readily for simple cases like rare gas dimers which bind because of dispersion. However, it can be difficult to understand the interaction for a more complicated system such as a complex formed by cationic halogenated benzene radical and water, where other intermolecular terms such as electrostatics, polarization, and charge transfer are all in play.

Modern quantum chemical methods are able to predict most intermolecular binding energies quite accurately, but there lacks a direct bridge between these energies and chemical concepts.[11] To this end, energy decomposition analysis (EDA)[12–14] aims to unravel the origin of the interaction by decomposing the binding energy into chemically motivated components. Admittedly, the resulting decomposition cannot be uniquely defined in the overlapping regime, and consequently there are multiple approaches in the literature for providing chemical interpretations of molecular complexes. Important seminal EDA schemes include the Kitaura-Morokuma (KM)-EDA that decomposes the Hartree-Fock (HF) interaction energy into electrostatic, Pauli repulsion, polarization and charge transfer contributions,[15–17] and the extended transition state (ETS) method developed by Ziegler and Rauk, which partitions interactions calculated from density functional theory (DFT) into electrostatics, Pauli repulsion, and orbital interaction.[18,19]

A significant improvement to the KM-EDA for HF and DFT was made possible by the variational treatment of polarization, accomplished via imposing a fragment-blocking constraint on the molecular orbital (MO) coefficient matrix.[20,21] Solving the resulting constrained variational equations leads to absolutely localized MOs (ALMOs)[22] that are used in the Block-Localized Wavefunction EDA (BLW-EDA)[23–25] and the ALMO-EDA[26–28] approaches, both of which separate the interaction energy into a “frozen" term and allow for separability of general induction into the polarization and charge transfer contributions. The frozen energy corresponds to the interaction between monomers with their MOs optimized for each isolated fragment, the polarization energy is then defined by the relaxation of each fragment's MOs in the presence of other fragments, and finally charge transfer corresponds to the energy lowering resulting from inter-fragment orbital mixing. Furthermore, each intermediate energy exhibits correct asymptotic behavior and is a well-defined variational quantity. Recently a second generation ALMO-EDA[28] was developed, which includes two further improvements: first, the frozen term can be further decomposed into contributions from Pauli repulsion, permanent electrostatics, and dispersion;[29] and second, the use of a ba-

sis constructed from fragment electric response functions (FERFs) in the ALMO-constrained SCF calculation enables a well defined basis set limit for the separation between polarization and charge transfer.[30] The resulting second generation ALMO-EDA scheme[28] also permits any underlying representation with no restriction to atomic orbitals. Other recent advances in ALMO-EDA include decomposition of molecular properties[31] and an extension to singly excited-state methods.[32,33]

In principle, EDAs can be extended to more accurate interaction energies obtained from correlated wavefunctions methods.[34] The simplest correlation method is second-order Møller-Plesset perturbation theory (MP2), which is accurate and widely used for molecular interactions such as hydrogen bonding,[35,36] as well as being fast and efficient with the use of density fitting or resolution of the identity (RI).[37,38] MP2 also performs well for radical-solvent interactions,[39] provided that a restricted open shell reference is used when the HF reference is spin-contaminated. The KM scheme has been extended to post-HF methods such as MP2, by assigning the entire contribution from correlation energy to dispersion.[40] However, the inclusion of correlation also has an effect on electrostatic interactions, polarization and charge transfer,[41,42] and thus other EDAs were developed to understand the full correlation effects on intermolecular binding. The local second-order Møller-Plesset perturbation theory (LMP2) approach naturally allows for a decomposition of the correlation energy into an intramolecular correlation, a dispersion and an ionic contribution.[43] However, MP2 can overestimate binding in dispersion-dominated interactions like π-stacking,[44–47] while coupled cluster theory provides significantly higher accuracy if triples are included (e.g. via CCSD(T)), albeit at significant computational cost. A similar concept to LMP2 has been applied at the CCSD(T) level to define the Local Energy Decomposition (LED) scheme, which distinguishes between intra- and intermolecular correlation contributions.[48–51] Perhaps the most widely used EDA approach is symmetry-Adapted Perturbation Theory (SAPT), which computes the interaction energy via a perturbative expansion starting with non-interacting fragments. High-level SAPT with intramolecular correlation taken into account can yield accuracy comparable to

CCSD(T),[52] and it decomposes the interaction energy into an electrostatic, an exchange, an induction and a dispersion term.[53–56]

We have developed an alternative post-HF approach, the ALMO-MP2-EDA scheme,[42,57] which builds on local correlation models[58,59] and on an earlier pilot effort[60] which did not correct the mean-field frozen and polarization terms for the effect of correlation. The original ALMO-MP2-EDA scheme was designed to decompose the correlation energy into the same terms as the mean-field ALMO-EDA scheme through the addition of an explicit dispersion term. The core idea was to assign the excitations that contribute to the MP2 energy into different classes (see Fig. 1): intra-fragment for frozen and polarization, charge conserving for dispersion and charge transferring for charge transfer. However, the previous ALMO-MP2-EDA scheme and implementation were both limited to interactions between closed-shell molecules. In this work the ALMO-MP2-EDA scheme is generalized to unrestricted and restricted open-shell MP2 to permit the study of intermolecular interactions of radicals with a correlated wavefunction method, for which DFT methods are shown to be error prone.[39,61] We verify that the correct asymptotic behaviour of frozen, polarization, dispersion and charge transfer is operative, and the method is applied to understand the hydration of halogenated benzene radical cations.,[62] as well as the different interaction motifs of the $CO_2^{-\bullet}$ radical anion with N-heterocycles in the gas phase.[63,64]

2 Theory

The notation used in this manuscript employs indices i, j, k, ... for occupied orbitals, a, b, c, ... for virtual and p, q, r, ... for either. As far as possible, the discussion is presented in the spin-orbital basis. However, at some points we specifically discuss unrestricted spatial orbitals where $\bar{p}$ represents the β spin space. Labels for fragments are denoted as A, B, C ... and P, Q, R refer to the auxiliary (RI) basis functions.

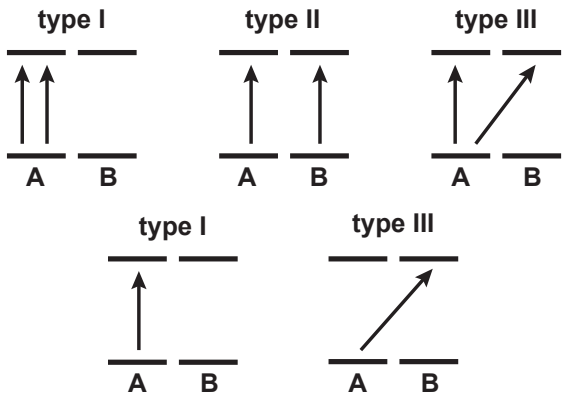

Figure 1: A representation for each of the three types of double excitations for a two-fragment system (A and B): on fragment (type I), charge conserving (type II) and charge transferring (III). In the case of RMP2 single excitations are also included, for which the on fragment and charge conserving constraints are identical. The lower level represents the occupied space and upper level the virtual space of each fragment.

2.1 Summary of MP2 Theory

The Hylleraas functional, J_H, is a variational formulation that when minimized yields the first order wave function and MP2 energy. The Fock operator ($\hat{F}$) is the usual choice for the zeroth-order Hamiltonian:[65–67]

$$J_H[\tilde{\Psi}] = \left\langle \Psi^{(0)} \middle| V - E^{(0)} \middle| \tilde{\Psi} \right\rangle + \left\langle \tilde{\Psi} \middle| H^{(0)} - E^{(0)} \middle| \tilde{\Psi} \right\rangle + \left\langle \tilde{\Psi} \middle| V - E^{(1)} \middle| \Psi^{(0)} \right\rangle \tag{1}$$

or in a more compact matrix-vector notation:

$$J_H[\tilde{\mathbf{t}}] = \tilde{\mathbf{t}}^\dagger \boldsymbol{\Delta} \tilde{\mathbf{t}} + \tilde{\mathbf{t}}^\dagger \mathbb{I} + \mathbb{I}^\dagger \tilde{\mathbf{t}} \tag{2}$$

Here $\tilde{\mathbf{t}}$ is a vector composed of the wave function amplitudes, $\tilde{t}_{ij}^{ab}$, $\mathbb{I}$ is a vector composed of two-electron integrals, $\langle ij||ab\rangle$, and $\boldsymbol{\Delta}$ is a supermatrix whose elements are defined as:

$$\Delta_{\binom{ab}{ij},\binom{cd}{kl}} = \left\langle \Psi_{ij}^{ab} \middle| \hat{F} - E^{(0)} \middle| \Psi_{kl}^{cd} \right\rangle \tag{3}$$

Unlike restricted or unrestricted MP2, the choice of the zeroth-order Hamiltonian is not

unique for ROHF, and, consequently, there are multiple approaches to MP2 with restricted open-shell HF references. Those approaches include ROMP2 by Amos *et al.*,[68] OPT1 and OPT2 by Murray and Davidson,[69] HCPT by Hubač and Čársky,[70] Z-averaged PT (ZAPT) by Lee and Jayatilaka,[71] RMP2 by Knowles and co-workers[72] and ROHF-MBPT2 by Bartlett and co-workers.[73] This paper follows the RMP2 approach of Knowles *et al.*[72] where the occupied-occupied and virtual-virtual blocks of the pseudo-canonicalized $\hat{F}^{\alpha}$ and $\hat{F}^{\beta}$ are defined as the zeroth-order Hamiltonian. This results in similar equations to unrestricted MP2 (UMP2). However, Brillouin's theorem does not hold and therefore singles contributions are included in the first-order MP wave function, yielding the following open-shell RMP2 energy expression:

$$E^{(2)} = -\sum_{ia} t_i^a F_{ai} - \frac{1}{4}\sum_{ijab} t_{ij}^{ab} \langle ij||ab\rangle \tag{4}$$

Here as usual $\langle ij||ab\rangle = (ia|jb) - (ib|ja)$. After pseudo-canonicalization, the singles and doubles amplitudes are defined as

$$t_i^a = \frac{F_{ai}}{\epsilon_a - \epsilon_i} \tag{5}$$

$$t_{ij}^{ab} = \frac{\langle ij||ab\rangle}{\epsilon_a + \epsilon_b - \epsilon_i - \epsilon_j} \tag{6}$$

Of course in UMP2, $t_i^a = 0$. In RMP2, the energy is spin-pure (though the amplitudes are not).

We will also use the RI approximation for the two-electron integrals:

$$(ia|jb) \simeq \sum_{Q}^{N_{\text{aux}}} \left[\sum_{P}^{N_{\text{aux}}} (ia|P)(P|Q)^{-1/2}\right] \left[\sum_{R}^{N_{\text{aux}}} (Q|R)^{-1/2}(R|jb)\right] \tag{7}$$

$$= \sum_{Q}^{N_{\text{aux}}} B_{ia}^{Q} B_{jb}^{Q}$$

2.2 The MP2-EDA Scheme

The total binding energy is defined as the energy difference between the complex and the isolated non-interacting fragments. It can be divided into a geometry distortion term, which is the energy required to deform isolated fragments from their optimum geometry to their geometry in the complex, and the interaction energy at the supersystem geometry (ΔE_{INT}). This interaction energy can be further partitioned into a mean-field contribution ΔE_{INT}^{HF} and a correlation contribution ΔE_{INT}^{MP2}. In this work, the mean-field contribution is decomposed using the original ALMO-EDA scheme:[26]

$$\Delta E_{INT}^{HF} = \Delta E_{FRZ}^{HF} + \Delta E_{POL}^{HF} + \Delta E_{CT}^{HF} \tag{8}$$

The frozen and polarized intermediate energies are evaluated using constrained HF wave functions. At the frozen level, a single determinant is constructed by combining the isolated fragments into a supersystem using *unrelaxed* fragment MOs. This captures the HF-level electrostatic and Pauli repulsion contributions. For polarization, the MOs are variationally optimized subject to the fragment-blocking constraint, leading to polarized ALMOs from solving the locally projected SCF scheme (SCF-MI).[20–22,74] This allows the electron densities on each fragment to adjust to the supersystem environment and naturally excludes charge transfer, which is finally obtained using the unconstrained HF energy.

The MP2 correlation energy is decomposed into the same terms by enforcing similar constraints; however, an additional term for dispersion naturally arises:[42]

$$\Delta E_{INT}^{MP2} = \Delta E_{FRZ}^{MP2} + \Delta E_{POL}^{MP2} + \Delta E_{DISP}^{MP2} + \Delta E_{CT}^{MP2} \tag{9}$$

The intermediate energies are presented in this section, largely following the notations used previously[42] where energies are given parenthetical labels that indicate (system-size/basis-type) at each stage of the analysis. System-size will be either "frag" for a fragment, or "sys"

for the supersystem.

At the mean-field level both frozen and polarized wave functions are constructed using fragment-blocked ALMO orbitals. The molecular orbitals in this basis are only orthogonal *within* each fragment. However, the MP2 energy expression is only well-defined for separated occupied and virtual spaces. Thus, both the frozen orbitals and converged ALMOs need to be properly prepared by projecting the occupied subspace out of the virtual orbitals. The occupied orbitals are then symmetrically orthonormalized[75] (globally) and the virtual orbitals are symmetrically orthonormalized on each fragment after being projected against the occupied space, yielding the pFRZ and pALMO basis, respectively.[42] The MP2 contribution to frozen energy, which captures the pure electrostatic effects and Pauli repulsion, is obtained using

$$\Delta E_{\mathrm{FRZ}}^{\mathrm{MP2}} = \sum_{A}^{N_{\mathrm{frag}}} E_{\mathrm{frz}}(\mathrm{frag/pFRZ})_A - \sum_{A}^{N_{\mathrm{frag}}} E_{\mathrm{iso}}(\mathrm{frag})_A - \mathrm{ABSSE} \tag{10}$$

where $E_{\mathrm{iso}}(\mathrm{frag})_A$ is the standard MP2 energy of each fragment evaluated in the canonical basis and ABSSE refers to the auxiliary basis set superposition error (*vide infra*). The frozen MP2 energy of each fragment, $E_{\mathrm{frz}}(\mathrm{frag/pFRZ})_A$, is obtained by freezing both fragment orbitals and t-amplitudes. The Hylleraas functional is employed to evaluate the MP2 energy with non-stationary t-amplitudes, using the full system frozen Fock matrix in the pFRZ MO basis for each fragment.

However, the MP2 wave function is not stationary with respect to occupied-virtual (ov) orbital rotations (θ_{ai}). As a consequence, the relaxed second-order density matrix incorporating first-order orbital response effects is required for evaluting the frozen energy (see previous work by some of us for a more detailed derivation[42]). The final expression for the frozen energy has the following form:

$$E_{\mathrm{frz}A} = J_H[\mathbf{t}_{\mathbf{A}}^{\mathbf{iso}}, \mathbf{C}_A, \mathbf{F}_A] - 2\sum_{ia} P_{iaA}^{(2)} F_{iaA} \tag{11}$$

where $\mathbf{t}_\mathbf{A}^\mathbf{iso}$ refers to the isolated t-amplitudes in the canonical fragment basis, F_{iaA} is the frozen Fock matrix transformed into the pFRZ MO basis of each fragment, and the ov block of the second-order density matrix, $P_{ia}^{(2)} = -Z_{ia}$ (the so-called Z-Vector[76]). The Z-vector (Z_{ia}) is obtained by contracting the inverse of HF electronic hessian with the MP2 orbital gradient:

$$Z_{jb} = \sum_{ia} \left(\frac{\partial^2 E^{\mathrm{SCF}}}{\partial\theta_{ai}\partial\theta_{bj}} \right)^{-1} \frac{\partial E^{(2)}}{\partial\theta_{ai}} \tag{12}$$

The explicit expressions and derivations for these terms can be found elsewhere.[66,67,77]

For restricted open-shell MP2 methods like RMP2, the derivation of the Z-vector is more involved, and interested readers are referred to refs. 78,79. The important point is that the RMP2 CPSCF equation can be expressed in a form that is equivalent to UMP2 gradient theory. In summary, obtaining the frozen energy at the MP2 level requires calculating the t-amplitudes on each isolated fragment, evaluating the Hylleraas functional and solving a CPSCF equation for each fragment.

Next, the MP2 contribution to polarization energy is obtained using

$$\Delta \mathrm{E}_{\mathrm{POL}}^{\mathrm{MP2}} = \sum_{A}^{N_{\mathrm{frag}}} \mathrm{E}_{\mathrm{pol}}(\mathrm{frag/pALMO})_A - \sum_{A}^{N_{\mathrm{frag}}} \mathrm{E}_{\mathrm{frz}}(\mathrm{frag/frz})_A \tag{13}$$

After the SCF-MI is converged the ALMOs on each fragment are transformed into the pALMO basis. The ALMO basis allows the assignment of molecular orbitals to fragments. The polarization constraint, like the frozen system, permits only paired double substitutions on the same fragment. This allows for obtaining $\mathrm{E}_{\mathrm{pol}}$(frag/pALMO) with standard MP2 energy evaluation using the pALMO basis of each fragment.

The dispersion energy is obtained using

$$\Delta \mathrm{E}_{\mathrm{DISP}}^{\mathrm{MP2}} = \mathrm{E}_{\mathrm{ccc}}(\mathrm{sys/ALMO}) - \sum_{A}^{N_{\mathrm{frag}}} \mathrm{E}_{\mathrm{pol}}(\mathrm{frag/ALMO})_A \tag{14}$$

where the charge conserving correlation (CCC) constraint is imposed. This constraint only

permits excitations that conserve the charge on each fragment as shown in Fig. 1 (types I and II). The CCCMP2 energy (E_{ccc}(sys/ALMO)) is evaluated for the whole system in the pALMO basis, which is neither orthonormal nor canonical. The derivative of the Hylleraas functional with respect to the amplitudes yields a set of linear equations to obtain the MP2 amplitudes:

$$\frac{\partial J_H^{\mathrm{CCC}}}{\partial \mathbf{t}^{\mathrm{CCC}}} = 0 \Rightarrow \mathbf{\Delta}^{\mathrm{CCC}}\mathbf{t}^{\mathrm{CCC}} = \mathbb{I}^{\mathrm{CCC}} \tag{15}$$

$$\sum_{i'j'a'b'} (\Delta^{\mathrm{CCC}})_{\binom{ab}{ij},\binom{a'b'}{i'j'}} (t^{\mathrm{CCC}})_{i'j'}^{a'b'} = \langle ij||ab\rangle^{\mathrm{CCC}} \tag{16}$$

where $\mathbf{\Delta}$ represents an 8 $^{\mathrm{th}}$-rank tensor that has the following form:

$$\left(\Delta^{\mathrm{CCC}}\right)_{\binom{ab}{ij},\binom{a'b'}{i'j'}} = -F_{ii'}g_{aa'}g_{jj'}g_{bb'} + g_{ii'}F_{aa'}g_{jj'}g_{bb'} - g_{ii'}g_{aa'}F_{jj'}g_{bb'} + g_{ii'}g_{aa'}g_{jj'}F_{bb'} \tag{17}$$

where $g_{rr'}$ refers to the MO-overlap matrix.

Utilizing the internal structure of $\mathbf{\Delta}$ tensor arising from the properties of the basis as well as the CCC constraint ($ia \in A$, i.e., pairs must be on the same fragment) simplifies the contraction on the left-hand side of Eq. 16. An efficient iterative algorithm to solve Eq. 16 was developed previously and is applied here as well.[57] The coupling terms $\left((\Delta^{\mathrm{CCC}})_{\binom{ab}{ij},\binom{a'\bar{b}'}{i'\bar{j}'}}\right)$ for the same-spin (t_{ij}^{ab}) and opposite-spin ($t_{i\bar{j}}^{a\bar{b}}$) blocks of the t-amplitudes are zero. As a consequence, the three spin blocks of the t-amplitudes can be solved independently. In contrast to the same-spin case, the opposite-spin $\mathbf{\Delta}$ tensor has no symmetry between the first and third or between the second and fourth terms, rendering the contraction over the opposite-spin amplitudes in Eq. 16 twice as costly. Finally, the energy is obtained by contracting the amplitudes with the charge-conserving two-electron integrals in the pALMO basis. For RMP2, we also need to include the contribution from the singles.[72] The CCC constraint for singles is identical to the on-fragment constraint. Therefore, the singles contribution from the polarization calculation is added to obtain E_{ccc}.

At last the MP2 contribution to charge transfer energy can be evaluated using

$$\Delta E_{CT}^{MP2} = E(sys) - E_{ccc}(sys/ALMO) - BSSE + ABSSE \tag{18}$$

where E(sys) corresponds to the full MP2 energy of the supersystem, BSSE to the standard basis set superposition error in MP2 correlation energy calculated from applying a counterpoise correction,[80] and ABSSE to the auxiliary basis set superposition error, which corresponds to the difference between isolated fragment MP2 energies evaluated with and without auxiliary basis function on the ghost atoms.[42]

3 Computational Details

All geometries were fully optimized with ωB97X-D[81]/def2-TZVPPD[82,83] and with an ECP for iodine[84] in the gas phase. The aug-cc-pVTZ basis set[85–87] in combination with the corresponding auxiliary basis[88,89] was employed for the MP2-EDA calculations. Reference calculations for the interaction energies were performed with the double-hybrid ωB97M(2) functional[90] with either the def2-QZVPPD or def2-TZVPPD basis set,[83] with their corresponding auxiliary basis set and an ECP for iodine.[84,91]

The electron density plots were visualized with an isovalue of 0.1 a.u., and a smaller isovalue (0.001 a.u.) was used for the density difference plots. A further analysis of CT using complementary occupied-virtual orbital pairs (COVPs)[92] is currently only available for mean-field methods, and thus we used EDA results with the ωB97M-V functional[93] to generated the COVPs (with an isovalue of 0.05 a.u.). ωB97M-V has been identified as one of the most accurate density functionals for intermolecular interactions by recent extensive benchmarks.[94,95] Furthermore, the calculated ωB97M-V interaction energies were similar to the RMP2 results (see Tables S4 and S6 in the Supporting Information (SI)).

3.1 Implementation Details

We implemented the EDA scheme for RMP2 (UMP2) in a development version of the Q-Chem 5 package,[96] which comprises the following steps:

1. Perform fragment ROHF (UHF) and subsequently canonical MP2 calculations based on these references.

2. Evaluate the frozen HF energy and compute E_{frz} for each fragment (Eq. 11).

3. Perform an ROSCF-MI (USCF-MI) calculation enforcing fragment-blocking of the MO coefficients and subsequently evaluate E_{pol} for each fragment.

4. Iteratively solve for the CCC t-amplitudes and evaluate E_{ccc}.

5. Perform a fully relaxed ROSCF (USCF) calculation for the supersystem followed by a canonical MP2 calculation.

6. Perform ROSCF (USCF) and canonical MP2 calculations for each individual fragment with other fragments as ghost atoms for BSSE and ABSSE corrections.

In cases where the radical is a single atom (e.g. $Cl^{\bullet}$) or of a highly symmetric geometry (e.g. $^{\bullet}OH$), there can be multiple degenerate electronic configurations with the unpaired electron residing in different orbitals, yielding non-uniquely defined frozen states as illustrated by the $Cl^{\bullet}\cdots H_2O$ complex in Fig. 2. For such systems, it is desirable to obtain the orientation of fragment spin that yields the most favorable frozen energy. We achieve this by *recalculating* the isolated fragments after the SCF-MI step with the corresponding block of the ALMO coefficient matrix as the initial guess in combination with the Maximum Overlap Method (MOM).[97] Note that the proper alignment of the radical was suggested in the EDA scheme for chemical bonds previously developed by Levine *et al.*[98,99] To obtain the Z-vectors, we iteratively solve a CPSCF equation (either RO or U) for each fragment which avoids the direct inversion of the electronic hessian.

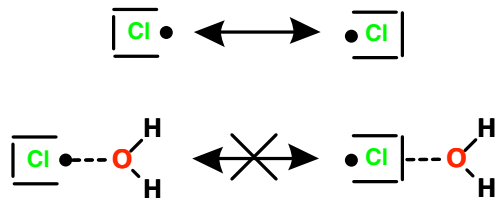

Figure 2: Illustration of the degenerate electronic configuration of the $Cl^{\bullet}$ radical, which then yields distinct frozen energies for the $Cl^{\bullet}\cdots H_2O$ complex depending on the initial orientation of the $Cl^{\bullet}$ spin density.

The linear equation to obtain the three sets of t-amplitudes (Eq. 16) follows an adaption of the efficient procedure of the closed-shell MP2-EDA scheme.[57] The initial guess is the t-amplitudes of the polarization calculations and a diagonal preconditioner is used to accelerate convergence. The construction of the charge conserving two-electron integrals for CCCMP2 follows a modified approach:

- Loop over all fragment pairs (AA, AB, AC, ...)
- For a given fragment pair AB, construct an intermediate $\mathbf{W}$ containing all two-electron integrals of the given fragment subspaces $W^{AB} = (i^A a^A | \bar{j}^B \bar{b}^B)$:

$$\mathbf{W}^{AB} = \mathbf{B}^{Q\dagger}_{ai\in A} \cdot \mathbf{B}^{Q}_{\bar{b}\bar{j}\in B}$$

- Map each $\mathbf{W}^{AB}$ into the $\mathbb{I}^{\mathrm{CCC}}$ tensor

All parts of the code are parallelized using a shared-memory programming model (OpenMP). The correct behavior of all terms were verified with simple test cases (see SI Sec. S1). The correct long-range decay of the polarization ($1/r^4$) was confirmed using an isolated lithium atom ($Li^{\bullet}$) interacting with an external charge. The correct long-range behavior of dispersion ($1/r^6$) and charge transfer (exponential) were confirmed with $He\cdots Li^{\bullet}$ complex (see SI Figs. S1(a)–(d)).

4 Results

The method is first applied to the binary radical-solvent complexes from the TA13 benchmark set.[39] Next, we use this method to investigate the first solvation step of cationic halogenated benzene radicals. As the final example, we study the different interaction motifs of a $CO_2^{-\bullet}$ radical with N-heterocycles (pyridine and imidazole) in the gas phase. With UMP2, there is spin contamination in at least one example in all three sets of applications: HF$-$CO$^+$ in the TA13 benchmark set ($\langle S^2 \rangle = 0.83$), the halogen-bonded chlorobenzene radical cation–water complex ($\langle S^2 \rangle = 0.88$), and the Py$-CO_2^{-\bullet}$ complex ($\langle S^2 \rangle = 0.94$). Furthermore, the RMSDs of UMP2 and RMP2 for the TA13 benchmark set (8.9 and 6.9 kJ/mol, respectively) suggest that RMP2 yields more accurate interaction energies. Hence, the following discussion focuses on the RMP2-EDA results only, which are also consistent with DFT-EDA (ωB97M-V) results (Tables S4 and S6 in the SI).

4.1 TA13 Benchmark Set

The TA13 benchmark set[39] includes thirteen binary radical-solvent complexes with non-bonded interactions, which are considered to be challenging non-covalent interactions for DFT due to a prominent self-interaction error.[61,94,100,101] The popular B3LYP functional has an RMSD of 16.1 kJ/mol for the interaction energies, and ωB97M-V, the overall best-performing functional according to extensive benchmarking, has an RMSD of 11.5 kJ/mol.[94] Both UMP2 and RMP2 calculations were performed for the interaction energies on all 13 molecules with significantly smaller RMSD values of 8.9 and 6.9 kJ/mol (for full results see SI Tables S1 (U) and S2 (RO)), respectively. The UMP2 vs. RMP2 difference stems mainly from the CO$^+-$HF complex because UMP2 exhibits significant spin contamination ($\langle S^2 \rangle = 0.83$ for the complex and 0.93 for the CO$^+$ monomer). The correlation energy is significant in most cases: e.g., it accounts for $\sim 50\%$ of the binding energy for Al$-H_2O$. The frozen terms at the MP2 level are all positive as the perturbation theory tends to correct

for the overestimation of the dipole moments of the HF reference (see SI Table S2). The radical alignment scheme (see Sec. 3.1) is crucial for radicals with degenerate electronic configurations such as Cl−OH_2, for which there can be a difference up to 40 kJ/mol in the resulting frozen term otherwise, depending on how the fragment spins are aligned initially.

The RMP2-EDA results are presented in Table 1 and are categorized into three groups based on the interaction motifs: electron-rich metal-water complexes, electron-poor hemibonded complexes, and hydrogen-bonded complexes. Additional details are provided in Table S2 in the SI, such as the break-down into HF and correlation contributions. The electron-rich metal-water complexes (Li, Al, Be^+) display large polarization and relatively small charge transfer. This is already an interesting and surprising result, because it suggests that the strong interaction is primarily *non-bonded* rather than having a substantial covalent contribution, as had been inferred from natural bond orbital (NBO) analysis.[102] The optimized geometry of these complexes involves interaction of the O atom of water with the metal center, which is the main reason that CT from the electron-rich metal center to the solvent is somewhat suppressed. As a fraction of the binding energy, CT is most important for the Al−H_2O complex, which also has a prominent contribution from dispersion.

The interaction of the family of electron-poor hemibonded complexes is mainly driven by charge transfer. Both Cl– and Br–water complexes show a significant charge transfer contribution to overcome Pauli repulsion at the frozen level. The cationic carbonyl complex with HF also shows a large CT contribution. However, in contrast to the halogen complexes, its short bond distance (r(O-F) = 1.8 Å) results in a strongly repulsive frozen term and the charged fragment induces significant polarization. The $NH_3{}^+$−H_2O complex shows balanced contributions from all terms, which is more similar to the typical scenario of the hydrogen-bonded motifs.[26,103] The strong electrostatic interaction renders the frozen term already attractive as the charge on the $NH_3{}^+$ radical and dipole moment of the water are favorably aligned. The charge also results in significant polarization. The last member of this group, F−OH_2, exhibits the largest error among the RMP2 interaction energies in this benchmark

Table 1: RMP2-EDA results for the TA13 benchmark set evaluated with the aug-cc-pVTZ basis. Energies are in kJ/mol and r refers to the complex bond distance.

System	ΔE_{FRZ}	ΔE_{POL}	ΔE_{DISP}	ΔE_{CT}	ΔE_{TOT}	r(Å)
electron-rich metal-water complexes						
H_2O-Al	96.9	-86.1	-21.5	-16.7	-27.5	2.20
H_2O-Be^+	102.8	-306.9	-11.8	-42.7	-258.6	1.57
H_2O-Li	40.5	-66.2	-8.0	-11.5	-45.2	1.88
electron-poor hemibonded complexes						
H_2O-F	60.6	-9.5	-11.7	-36.3	3.1	2.11
H_2O-Cl	28.9	-7.1	-12.2	-19.7	-10.0	2.60
H_2O-Br	28.9	-8.5	-12.9	-17.6	-10.2	2.70
$HF-CO^+$	121.5	-101.8	-22.1	-117.4	-119.9	1.80
$H_2O-NH_3{}^+$	-14.3	-21.5	-12.3	-22.8	-70.8	2.32
hydrogen bonded complexes						
$HOH-CH_3$	6.8	-2.9	-5.5	-5.1	-6.7	2.33
$H_2O-HNH_2{}^+$	-3.2	-54.9	-13.5	-32.6	-104.2	1.54
$FH-BH_2$	11.1	-8.6	-5.6	-13.3	-16.4	2.22
$FH-NH_2$	12.9	-24.0	-9.9	-20.6	-41.7	1.75
FH−OH	5.7	-12.0	-6.6	-10.8	-23.7	1.81

set. This complex has significant static correlation and is consequently not very accurately described by MP2 (or DFT) methods as discussed in Ref. 39. Hence, the EDA terms are just reported for completeness.

The hydrogen-bonded complexes have more balanced contributions from all energy components including significant charge transfer similar to results reported for closed-shell hydrogen bonding.[31,103,104] However, there are variations in the weight of these terms: the importance of charge transfer (measured relative to the total interaction energy) is higher for the more electropositive radicals such as CH_3 and BH_2, while complexes of the more electronegative radicals (NH_2, OH and $HNH_2{}^+$) exhibit stronger attractive electrostatic interaction (resulting in a less repulsive frozen term) and more significant polarization.

4.2 Halogenated Benzene Radical Cation: Halogen or Hydrogen Bonding?

Ionic hydrogen bonds (IHBs) constitute a subclass of hydrogen bonding between radical ions and polar molecules with a binding energy ranging from -20 to -140 kJ/mol.[62,105] Halogen bonds are defined according to IUPAC as a linear binding motif R−X···Y where X denotes a covalently bonded halogen atom acting as a Lewis acid (electron-poor) and Y is an electron-rich Lewis base (e.g. halide anion, water, etc.).[106] Halogen bonding is a type of intermolecular interaction that in part arises from the favorable electrostatic interaction between the halogen atom and the acceptor (Lewis base), which is often described in terms of the so-called σ-hole.[107,108] However, many recent studies suggest that the $n \rightarrow \sigma^*$ charge transfer plays an important and even dominant role in halogen bonding.[109–114] While a consensus has almost been reached that permanent electrostatics alone is inadequate to describe halogen bonds, there is still an ongoing debate especially about the role of charge transfer.[108,109,111–116]

A recent study by El-Shall and co-workers discovered two competing mechanisms for the first hydration step of halogen-substituted benzene radical cations using mass-selected ion mobility spectroscopy. Depending on the halogen atom there is a preference for either IHBs, as depicted in Fig. 3(a), or ionic halogen bonds (IXBs), as depicted in Fig. 3(b).[62] The authors found that $C_6H_5F^{+\bullet}$ solely forms IHB while $C_6H_5I^{+\bullet}$ solely forms IXB, and the chloro- and bromobenzene radical cations show an equilibrium between IXB and IHB isomers.[62] The substituent dependence of the IHB vs. IXB competition makes this class of systems interesting candidates for an EDA analysis. These insights on the control of halogen bonding strengths can be useful for the design of new catalysts.[117]

The RMP2-EDA was employed to understand the competition between IHB and IXB in complexes of H_2O with $C_6H_5X^{+\bullet}$: a total of eight different isomers were analyzed. As an example, the optimized geometries of the IHB and IXB complexes formed by bromobenzene are shown in Fig. 4. All RMP2 interaction energies are in good agreement with the results of an accurate double-hybrid functional (ωB97M(2)) with the def2-TZVPPD basis (see SI

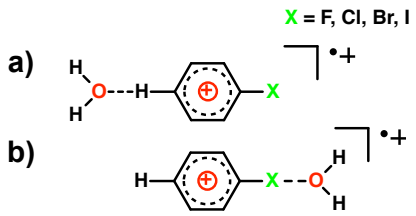

Figure 3: Two competing binding motifs for the interaction between a halogenated benzene radical cation ($C_6H_5X^{+\bullet}$) and a water molecule: (a) Ionic hydrogen bonding (IHB) and (b) ionic halogen bonding (IXB).

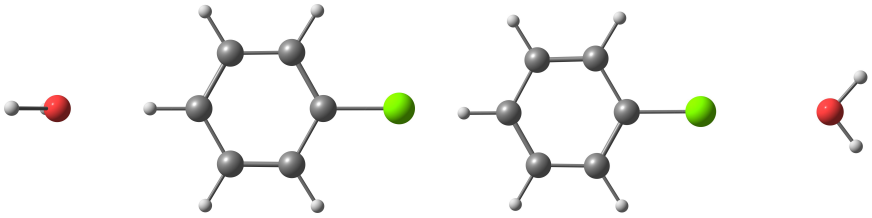

(a) (b)

Figure 4: Optimized geometries for two isomers of the halogenated benzene radical cation–water complex: (a) the IHB structure ($r_{H\cdots O}$ in Å: F: 2.02, Cl: 2.04, Br: 2.05, I: 2.08); (b) the IXB structure ($r_{X\cdots O}$ in Å: F: 2.97, Cl: 2.78, Br: 2.78, I: 2.83).

Table S3). Furthermore, it is verified that the trends in both the total interaction energies and the individual energy components are consistent with the results of DFT-based ALMO-EDA with ωB97M-V (see SI Table S4).

The full results for the bromobenzene–water complex are shown in Fig. 5, whose IHB and IXB isomers are of the closest total interaction energies (with the IXB isomer being slightly more favorable by 2.8 kJ/mol) among all halogenated benzene radicals investigated here. The relative EDA energies with respect to fluorobenzene for both binding motifs are shown in Fig. 6, which help uncover the trends *within* each binding mode. Finally, the energy differences between IHB and IXB in the total interaction energies and each individual energy component is depicted in Fig. 7 to help understand the different binding preferences for each halogenated benzene radical cation.

The EDA results for the IHB bromobenzene radical cation (see the left panel of Fig. 5) show an interaction that is dominated by attractive frozen (due to permanent electrostatics) and polarization terms, and the contributions from dispersion and charge transfer are also

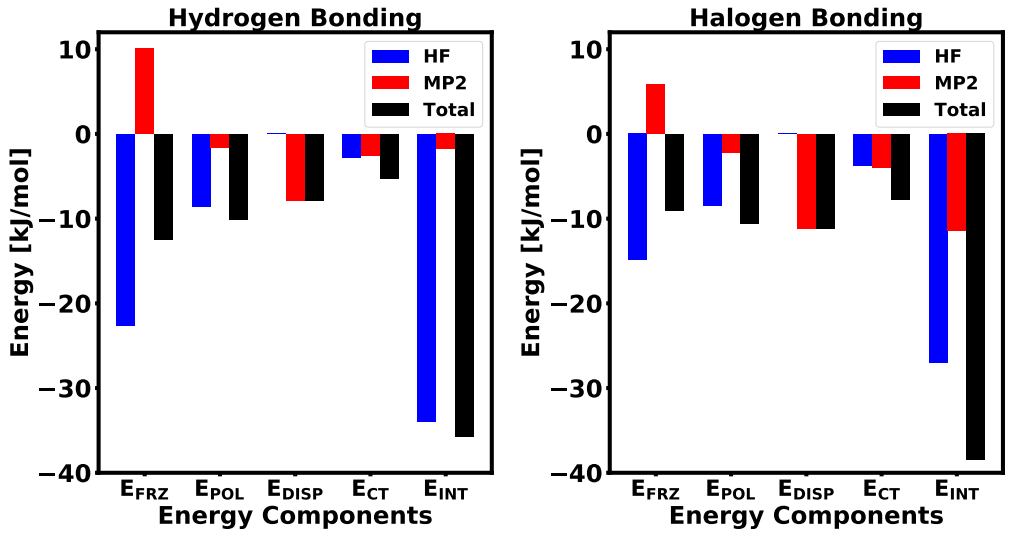

Figure 5: Individual EDA terms (in kJ/mol) for the two binding motifs of the water–bromobenzene radical cation complex, separated into HF and MP2 contributions.

not negligible. Although the MP2 contribution to the total IHB interaction energy is small, its contributions to the individual terms are not, especially its effect on the frozen term where MP2 corrects the overly attractive electrostatic interaction evaluated at the HF level.[41] The EDA results uncover a favorable error cancellation for the IHB motif at the HF level as the overestimated permanent electrostatic interaction compensates for the missing dispersion contribution that only arises at the MP2 level. The IXB motif has a more significant net MP2 contribution, and it is noteworthy that IXB is more favorable than IHB for this complex only when the effects of electron correlation are incorporated.

For the IHB isomers $H_2O\cdots C_6H_5X^{+\bullet}$, as shown in the left panel of Fig. 6, the magnitude of the total interaction energy monotonically decreases from lighter to heavier halogens. This trend stems mainly from the changes in the frozen and polarization terms (i.e. permanent and induced electrostatics), and can be readily rationalized with the increasing strength of the mesomeric effect (donating lone pairs to the benzene ring) of the halogens that makes the *para*-carbon more electron-rich and the C–H bond less polar. The CT term appears to be nearly independent of the halogen, which can be rationalized by analyzing the most important COVP. As shown in Fig. S2(a) in the SI, the CT in the IHB isomer is primarily

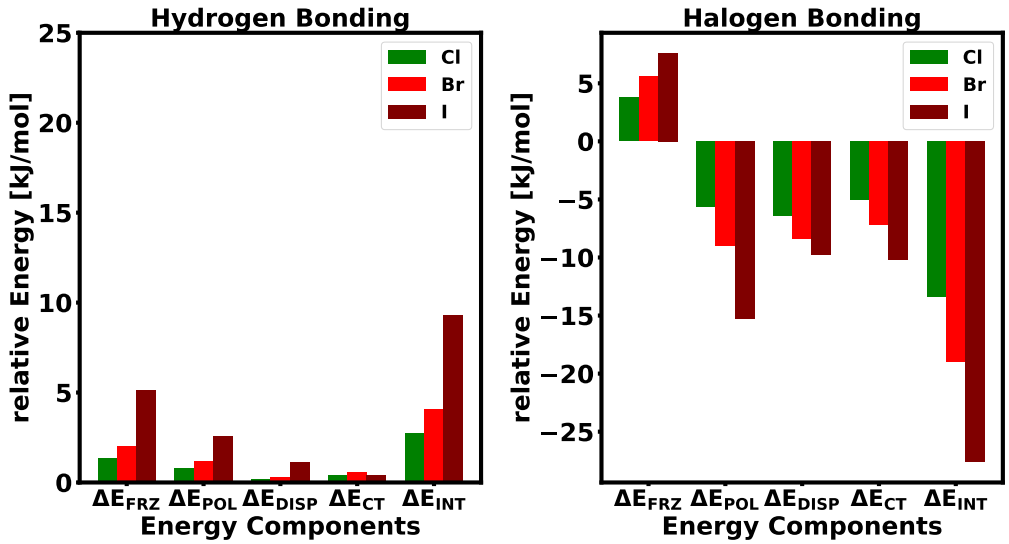

Figure 6: Changes in the total interaction energy and individual EDA terms for the heavier halogenated benzene radical cations relative to the fluorobenzene results with the two bonding motifs of the $H_2O\cdots C_6H_5X^{+\bullet}$ complexes.

from the oxygen lone pair on H_2O to the C−H σ^* orbital. This acceptor orbital is not strongly affected by the *para*-substitution.

The EDA results for the IXB bromobenzene (the right panel of Fig. 5) show significant contributions from all terms with polarization and dispersion being the most important contributions. The MP2 term has the same sign for E_{POL} and E_{CT} but has an opposite sign for the frozen term, for the reason discussed above. The importance of all interaction energy components (permanent electrostatics, polarization, dispersion, and charge transfer) to overcome the Pauli repulsion for the IXB binding motif is in line with the conclusion reached by a previous study on halogen bonding by some of us.[112]

As shown in Fig. 6, the IXB interaction energy increases strongly for the heavier halogens. The interaction with fluorobenzene is the weakest, and in fact, the IXB isomer for fluorobenzene could only be obtained with a symmetry constraint (C_{2v}) in the geometry optimization (i.e. it is not the global minimum on the PES). The increase in halogen bond strength is mainly attributed to an increase in polarization, dispersion and charge transfer. The increase in dispersion and polarization can be rationalized by the increasing softness and ionic radius down the halogen series. Interestingly, the frozen term exhibits an oppo-

site trend and is most favorable for the fluorobenzene, which is mainly attributed to the increase in Pauli repulsion as the halogen becomes more diffuse from F to I while the equilibrium X$\cdots$O distances do not change significantly (see the distances given in the caption of Fig. 4). The increase in charge transfer can be rationalized by analyzing the COVP (see SI Fig. S2(b)): the charge transfer is dominated by the donation from the oxygen lone pair to the C$-$X σ^* orbital whose energy is lowered (which facilitates CT) monotonically for the heavier halogens.

The comparison between the IHB and IXB isomers for each halogenated benzene radical cation is shown in Fig. 7, in which the differences (IHB $-$ IXB) in both the total interaction energy and each individual component are plotted. The IHB is more favorable than the IXB motif by over 20 kJ/mol for fluorobenzene, while the interaction energies of IHB and IXB are very similar for both Cl- and Br-substituted benzene radical cations. Iodobenzene, on the other hand, prefers the IXB motif by more than 27 kJ/mol. This trend can be explained by the increase of polarization, dispersion, and charge transfer of the IXB motif due to the increasing softness, atomic radius, and lower-lying C$-$X σ^* from F to I contrasting with the almost constant behavior of the hydrogen bonding side.

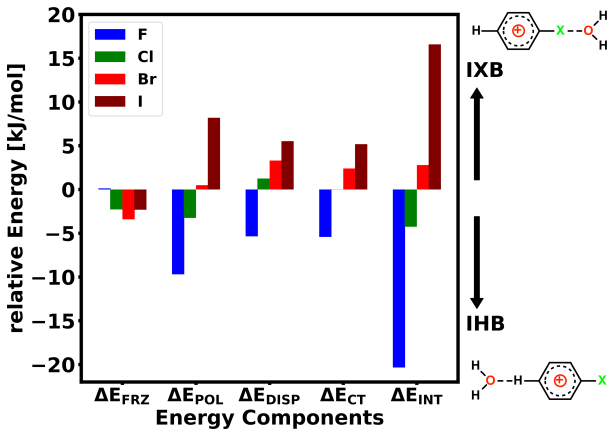

Figure 7: Term-by-term energy differences between the IHB and IXB binding motifs of the $H_2O\cdots C_6H_5X^{+\bullet}$ complexes.

4.3 Anionic CO_2 radical N-heterocycle complexes

Fossil fuel emission is yielding unprecedentedly high concentrations of CO_2 in the atmosphere, which acts as one of the main driving forces of global climate change. This has attracted considerable attention on artificial photosynthesis.[118,119] Both pyridine (Py), C_6H_5N, and imidazole (Im), C_3N_2H, are known to be active catalysts in the photoelectrochemical conversion of CO_2.[120,121] Interestingly, two distinct mechanisms are proposed for the initial CO_2 activation: pyridine forms a C−N bond via a carbamate intermediate; in contrast, imidazole forms a C−C bond with the C2 carbon.[121] In the quest for the elucidation of catalytic mechanisms, structural information about possible intermediates is both crucial and scarce.

Johnson and co-workers characterized possible intermediates via the reaction of both N-heterocycles with small anionic CO_2 clusters ($(CO_2)_m^{-\bullet}$, m=2−7)[122–124] in the gas phase. They obtained vibrational spectra of both anionic complexes: Py−$CO_2^{-\bullet}$ and Im−$CO_2^{-\bullet}$.[63,64] The stable carbamate Py−$CO_2^{-\bullet}$ radical anion (Fig. 8(a)) was discovered by the reaction of $(CO_2)_m^{-\bullet}$ clusters with pyridine in the gas phase.[63,125] The carbamate motif was identified via a C-N stretch feature in the vibrational predissociation spectra of Py−$CO_2^{\cdot-} \cdot (CO_2)_3$.[63] A similar study using imidazole instead of pyridine found a different interaction motif (Fig. 8(b)): hydrogen bonding of $CO_2^{-\bullet}$ to the H−N group yields a strong red-shift in the N-H stretching frequency.[64]

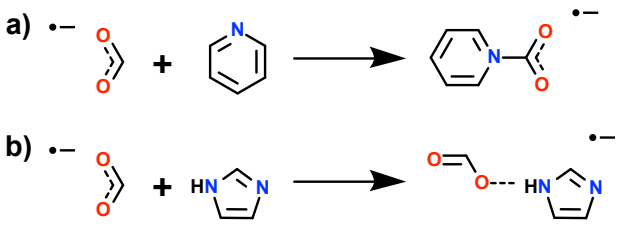

Figure 8: Different binding motifs for the association of a $CO_2^{-\bullet}$ with nitrogen heterocycles: (a) pyridine (Py) resulting in a carbamate radical anion and (b) imidazole (Im) resulting in hydrogen bonding.

Since the different nature of these interactions could be relevant to their different catalytic mechanisms, we employ RMP2-EDA to gain insights into these two distinct binding

motifs. In particular, by comparing the EDA results for the four complexes shown in Fig. 9 (Py$-CO_2^{-\bullet}$ and Im$-CO_2^{-\bullet}$ with two binding modes for each), we elucidate why different binding motifs are preferred by pyridine and imidazole. All RMP2 interaction energies are in good agreement with reference interaction energies calculated at the ωB97M(2)/def2-QZVPPD level of theory (see SI Table S5). Furthermore, the same trends in both the total interaction energies and the individual EDA terms are obtained using DFT-EDA with the ωB97M-V functional (see SI Table S6).

The calculated total binding energies are similar for Py$-CO_2^{-\bullet}$ and Im$-CO_2^{-\bullet}$, which are -140 and -104 kJ/mol, respectively. However, as shown in Fig. 10, the energy components reveal dramatically different nature of these interactions. The carbamate motif is strongly repulsive at the frozen level. This can be understood by the fact that the unpaired electron is localized in a CO_2 π^* orbital, which localizes most of the spin density on the carbon atom (see SI Fig. S3(a)). In addition, the C$-$N bond distance is very short at only 1.49 Å, rendering the frozen term dominated by the Pauli repulsion between the lone pair of the N atom and the π^* of the $CO_2^{-\bullet}$-fragment. The polarization term is strongly attractive, which is most likely due to the redistribution of charges on the $CO_2^{-\bullet}$ fragment induced by the lone pair on nitrogen. This effect can be rationalized by the electron density difference of $CO_2^{-\bullet}$ with and without a partial negative charge ($0.5e^-$) located 1.5 Å away from the carbon atom on the bisector, which demonstrates how an electronegative species redistributes the spin density from C to both O atoms (see SI Fig. S3(b)). CT also plays an important role in this interaction, and it is bidirectional with both forward and backward donations being significant. The spin density of the fully relaxed Py$-CO_2^{-\bullet}$ complex reveals a forward donation of the unpaired electron into the pyridine's π^* orbital (see SI Fig. S3(c)). However, the bent O$-$C$-$O angle indicates a reduced CO_2 fragment, implying significant backward CT from the lone pair into the CO_2 fragment. Note that polarization of the CO_2 fragment, as discussed above, makes the carbon more positive and thus more prone to nucleophilic attacks).

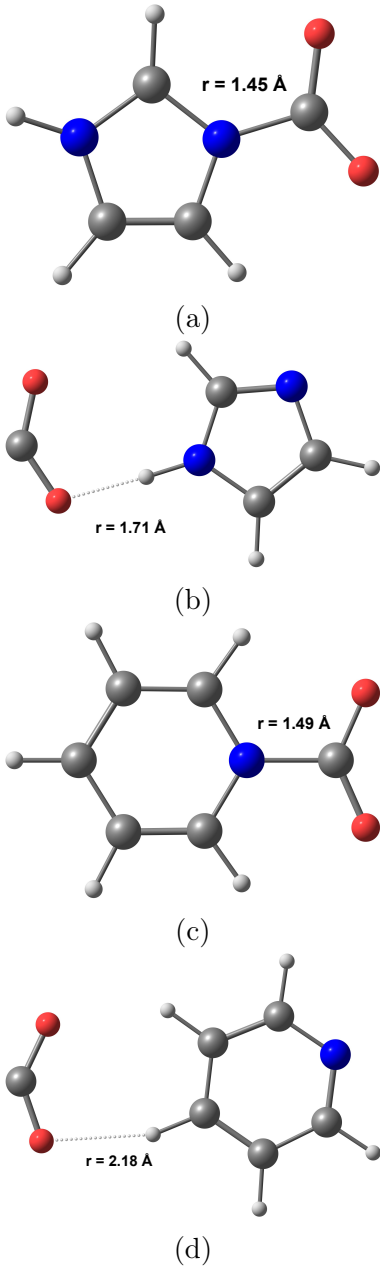

Figure 9: Geometries of the four possible isomers using both binding motifs for the reaction of a $CO_2^{-\bullet}$ with nitrogen heterocycles: (a) carbamate Im$-CO_2^{-\bullet}$; (b) hydrogen-bonded Im$-CO_2^{-\bullet}$; (c) carbamate Py$-CO_2^{-\bullet}$; (d) hydrogen-bonded Py$-CO_2^{-\bullet}$.

In contrast, the EDA fingerprints of the hydrogen-bonded Im$-CO_2^{-\bullet}$ complex (the right panel of Fig. 10) shows more balanced contributions from various components, which is similar to the IHB motifs discussed in Sec. 4.2. The O$-$H bond distance (1.71 Å) is slightly longer than the carbamate motif for Py$-CO_2^{-\bullet}$. The largest contribution comes from polarization,

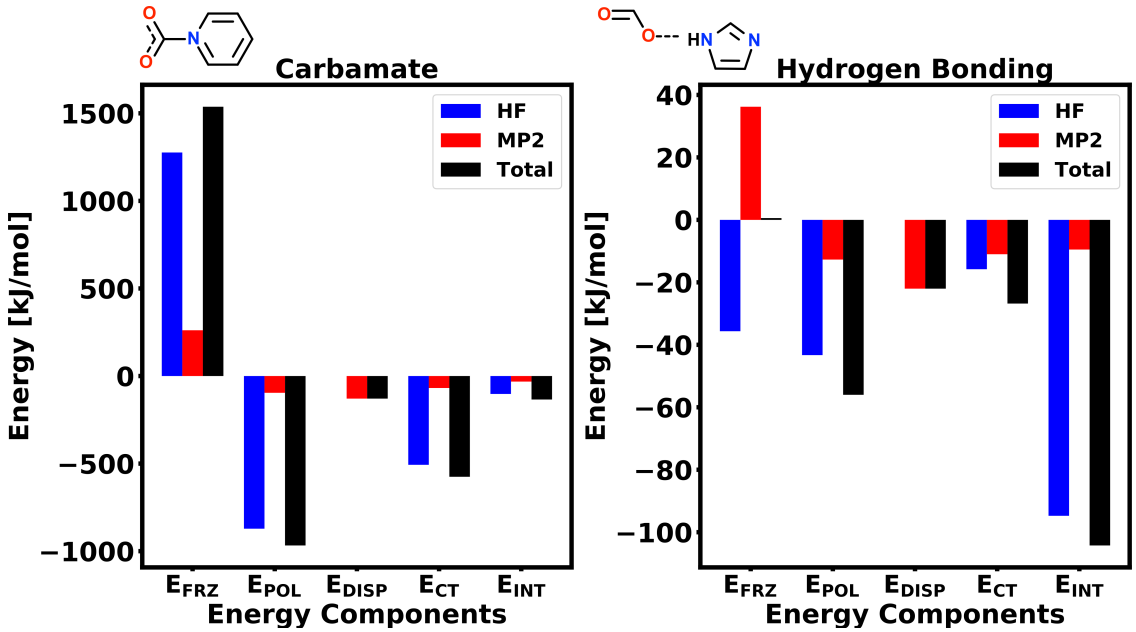

Figure 10: RMP2-EDA results (using the aug-cc-pVTZ basis) for the carbamate and hydrogen bonding motifs of $CO_2^{-\bullet}$, separated into HF and MP2 contributions.

followed by also significant contributions from dispersion and charge transfer. The dominant role of polarization can be readily rationalized by the anionic CO_2 fragment that has large polarizability and the polar N−H bond. Interesting, the HF and MP2 contributions to the frozen term almost perfectly cancel each other for this complex, rendering the overall frozen term close to zero.

The experimentally observed Py−$CO_2^{-\bullet}$ carbamate has an interaction energy of −146.4 kJ/mol as calculated with RMP2. By contrast, the imidazole carbamate (Fig. 9(a)) is far less stable with an interaction energy of only −20.7 kJ/mol. The EDA components of the imidazole carbamate relative to the pyridine results are shown in the left panel of Fig. 11. The frozen interaction is significantly more repulsive for imidazole carbamate, which, however, is almost fully compensated by its more favorable polarization energy. There is also a significant decrease in CT from pyridine to imidazole, even though the latter is a stronger base and thus should exhibit a stronger forward donation from the nitrogen lone pair to $CO_2^{-\bullet}$. The results imply that this is insufficient to compensate for the less favorable back donation of the $CO_2^{-\bullet}$ fragment into the π^* orbital of imidazole.

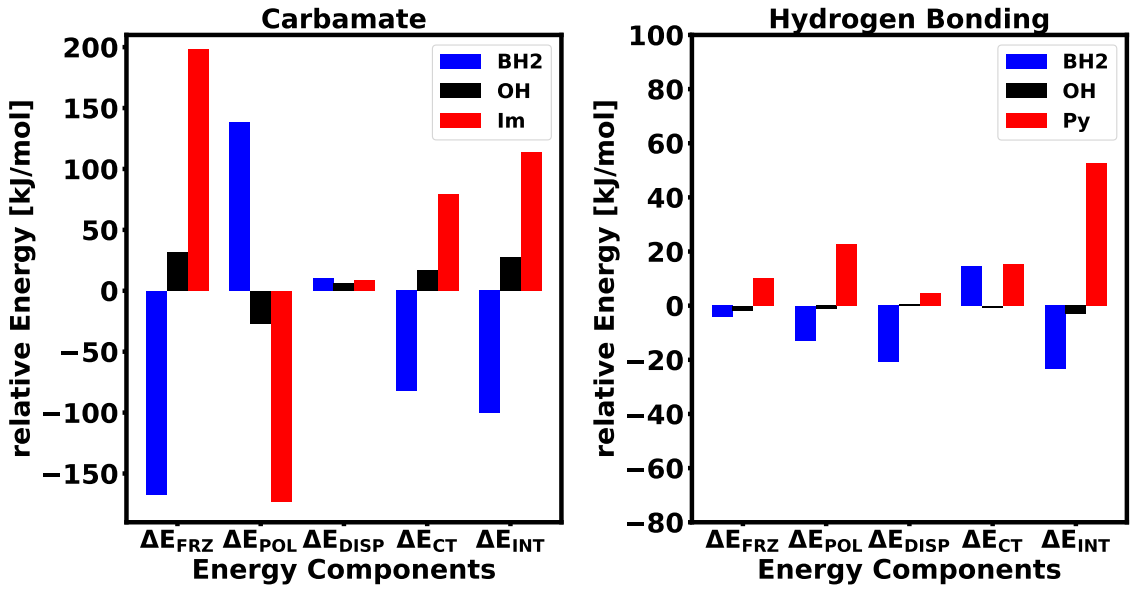

Figure 11: Left panel: comparison of the EDA components for the Py$-CO_2^{-\bullet}$ carbamate against those for its *para*-substituted (by $-$OH and $-BH_2$) derivatives and the imidazole carbamate; right panel: comparison of the Im$-CO_2^{-\bullet}$ hydrogen-bonded complex against the hydrogen binding of pyridine and its *para*-substituted derivatives with $CO_2^{-\bullet}$.

To probe the effect of substituent groups on the Py$-CO_2^{-\bullet}$ carbamate complex, we separately place an electron-donating hydroxyl ($-$OH) group and an electron-withdrawing $-BH_2$ group at the *para* carbon. The energy components relative to the unsubstituted pyridine results are plotted on the left panel of Fig. 11. The $-BH_2$ group yields a more electron-deficient aromatic system, strengthening the interaction energy by $\sim$100 kJ/mol. The comparison against the unsubstituted case manifests its less repulsive frozen term as well as a less favorable polarization contribution, for which the differences largely cancel each other. The $-BH_2$ group also facilitates the donation from $CO_2^{-\bullet}$ to the lowered π^* orbital, as reflected by the markedly stronger charge transfer stabilization. An opposite effect is observed with the $-$OH group, which has a positive mesomeric effect by donating electron to the π-system, and it reduces the interaction energy with $CO_2^{-\bullet}$ by 28 kJ/mol. This net decrease mainly stems from the more repulsive frozen interaction and the weaker donation from $CO_2^{-\bullet}$ to the π^* orbital.

The RMP2 results for experimentally observed hydrogen-bonded Im$-CO_2^{-\bullet}$ yields an in-

teraction energy of −104.2 kJ/mol, while the hydrogen-bonded Py−$CO_2^{-\bullet}$ complex (Fig. 9(d)) is only half as strongly bound (−51.5 kJ/mol). The EDA components of the hydrogen-bonded pyridine relative to the hydrogen-bonded imidazole complex are shown on the right panel of Fig. 11. All energy components are destabilized upon the replacement of imidazole by pyridine. The N−H bond is more polar than C−H, which explains the more favorable electrostatic interaction as well as the stronger polarization of $CO_2^{-\bullet}$ in the complex with imidazole. The COVPs reveal a donation from $CO_2^{-\bullet}$ into the N−H σ^* orbital, which is more favorable than the donation into the C−H σ^*, elucidating the difference in CT (see SI Fig. S4). This is similar to the trend observed in Sec. 4.2. In contrast to the carbamate motif, there is no clear substituent effect for the hydrogen bonding motif because the π system does not play a key role in this type of interaction as the same COVP implies.

5 Conclusion

In this work, we generalized the previously reported closed-shell MP2-EDA scheme[42,57] to unrestricted and restricted open-shell MP2. This permits decomposition of the correlation energy of intermolecular interactions of radical systems into frozen, polarization, dispersion and charge transfer components. The scheme is efficiently implemented using OpenMP parallelism. In the case of a single atom or small radical fragments where the unpaired electron is located in a non-spherically symmetric orbital (e.g. $Cl^{\bullet}$), a proper alignment of the radical at the isolated fragment stage is necessary for obtaining unambiguously defined frozen and polarization energies.

Restricted open-shell MP2 is able to provide reasonably accurate binding energies for the radical-neutral complexes contained in the TA13 benchmark set, for which DFT can be error prone due to the self-interaction problem. The EDA analysis revealed that the different bonding motifs are driven by different energy components: the electron-rich metal-water complexes by polarization, the electron-poor hemibonded complexes by charge transfer, and

the hydrogen bonded complexes show more balanced contributions from all terms.

The MP2-EDA was applied to study the first solvation step of halogenated benzene radical cations with water where two binding modes are possible: ionic hydrogen bonding and ionic halogen bonding. The EDA results show that IXB becomes more favorable as the halogen becomes heavier due to an increase in polarization, dispersion and charge transfer, whereas the IHB binding site is not strongly affected by the type of halogen. This makes the halogen bonding site more attractive for the iodobenzene-water complex.

Analysis of $CO_2^{-\bullet}$ interacting with pyridine as a carbamate and with imidazole via hydrogen bonding revealed very different fingerprints for these interactions. The carbamate shows very repulsive frozen interaction, strong polarization and bidirectional charge transfer. The hydrogen bonding motif exhibits balanced contributions from polarization, dispersion and charge transfer with a frozen term of very small magnitude. The carbamate motif is preferred by pyridine as it allows for a stronger charge transfer interaction, whereas the hydrogen bonding motif is preferred by imidazole because the more polar N−H bond results in stronger polarization of the $CO_2^{-\bullet}$ fragment. Furthermore, the importance of charge transfer into the π^* orbital of the heterocycle was discovered as a parameter to control the stability of the carbamate binding mode with a substituent effect.

While the MP2-EDA is already useful for chemical applications, as demonstrated by the examples presented here, further methodological development is still desirable in the future. Unlike the second generation ALMO-EDA for DFT that has a useful basis set limit for all terms,[28] our current MP2-EDA scheme does not have this desirable feature. We hope to lift this limitation in future work. Additionally, it would be highly desirable to extend this approach from MP2 to recently developed methods based on regularized orbital-optimized MP2 (OOMP2)[67,126,127] and double-hybrid density functionals.[90,128] Furthermore, extending it to higher-order MP approach using OOMP2 orbitals[129] as well as revisiting coupled-cluster methods[60] are needed when a more accurate description for electron-electron correlation effects is necessary.

Acknowledgement

This work was supported by the U.S. National Science Foundation through Grant CHE-1665315. We also acknowledge partial support from CalSOLV. MHG is a part-owner of Q-Chem Inc.

Supporting Information Available

Verification of the long-range decay behavior of each energy component; full UMP2- and RMP2-EDA results for the TA13 benchmark set; full RMP2-EDA results and additional analysis of electron density and COVPs for the halogenated benzene radical cation–water complexes and the interaction between CO_2 anionic radical and N-heterocycles. This material is available free of charge via the Internet at `http://pubs.acs.org/`.

References

(1) Stone, A. *The Theory of Intermolecular Forces*, second edition ed.; Oxford University Press: Oxford, 2013.

(2) Scheiner, S. *Noncovalent forces*; Springer, 2015; Vol. 19.

(3) Müller-Dethlefs, K.; Hobza, P. Noncovalent Interactions: A Challenge for Experiment and Theory. *Chem. Rev.* **2000**, *100*, 143–168.

(4) Rose, G. D.; Wolfenden, R. Hydrogen Bonding, Hydrophobicity, Packing, and Protein Folding. *Annu. Rev. Biophys.* **1993**, *22*, 381–415.

(5) Hubbard, R. E.; Kamran Haider, M. Hydrogen bonds in proteins: role and strength. *e LS* **2010**,

(6) Grabowski, S. J. What is the covalency of hydrogen bonding? *Chem. Rev.* **2011**, *111*, 2597–2625.

(7) Meyer, F.; Dubois, P. Halogen bonding at work: recent applications in synthetic chemistry and materials science. *CrystEngComm* **2013**, *15*, 3058–3071.

(8) Steiner, T. The Hydrogen Bond in the Solid State. *Angew. Chem. Int. Ed.* **2002**, *41*, 48–76.

(9) Toste, F. D.; Sigman, M. S.; Miller, S. J. Pursuit of Noncovalent Interactions for Strategic Site-Selective Catalysis. *Acc. Chem. Res.* **2017**, *50*, 609–615.

(10) Neel, A. J.; Hilton, M. J.; Sigman, M. S.; Toste, F. D. Exploiting non-covalent π interactions for catalyst design. *Nature* **2017**, *543*, 637–646.

(11) Neese, F.; Atanasov, M.; Bistoni, G.; Maganas, D.; Ye, S. Chemistry and Quantum Mechanics in 2019: Give Us Insight and Numbers. *J. Am. Chem. Soc.* **2019**, *141*, 2814–2824.

(12) Phipps, M. J.; Fox, T.; Tautermann, C. S.; Skylaris, C.-K. Energy decomposition analysis approaches and their evaluation on prototypical protein–drug interaction patterns. *Chem. Soc. Rev.* **2015**, *44*, 3177–3211.

(13) Pastorczak, E.; Corminboeuf, C. Perspective: Found in translation: Quantum chemical tools for grasping non-covalent interactions. *J. Chem. Phys.* **2017**, *146*, 120901.

(14) Zhao, L.; von Hopffgarten, M.; Andrada, D. M.; Frenking, G. Energy decomposition analysis. *WIREs: Comput. Mol. Sci.* **2018**, *8*, e1345.

(15) Morokuma, K. Molecular orbital studies of hydrogen bonds. III. C=O··· H–O hydrogen bond in H_2CO··· H_2O and H_2CO··· $2H_2O$. *J. Chem. Phys.* **1971**, *55*, 1236–1244.

(16) Kitaura, K.; Morokuma, K. A new energy decomposition scheme for molecular interactions within the Hartree-Fock approximation. *Int. J. Quantum Chem.* **1976**, *10*, 325–340.

(17) Morokuma, K. Why do molecules interact? The origin of electron donor-acceptor complexes, hydrogen bonding and proton affinity. *Acc. Chem. Res.* **1977**, *10*, 294–300.

(18) Ziegler, T.; Rauk, A. On the Calculation of Bonding Energies by the Hartree Fock Slater Method. *Theor. Chem. Acc.* **1977**, *46*, 1–10.

(19) Ziegler, T.; Rauk, A. A Theoretical Study of the Ethylene-Metal Bond in Complexes between Cu^+, Ag^+, Pt^0, or Pt^{2+} and Ethylene, Based on Hartree-Fock-Slater Transition-State Method. *Inorg. Chem.* **1979**, *18*, 1558–1565.

(20) Stoll, H.; Wagenblast, G.; Preuβ, H. On the use of local basis sets for localized molecular orbitals. *Theor. Chem. Acc.* **1980**, *57*, 169–178.

(21) Gianinetti, E.; Raimondi, M.; Tornaghi, E. Modification of the Roothaan equations to exclude BSSE from molecular interaction calculations. *Int. J. Quantum Chem.* **1996**, *60*, 157–166.

(22) Khaliullin, R. Z.; Head-Gordon, M.; Bell, A. T. An efficient self-consistent field method for large systems of weakly interacting components. *J. Chem. Phys.* **2006**, *124*, 204105.

(23) Mo, Y.; Gao, J.; Peyerimhoff, S. D. Energy decomposition analysis of intermolecular interactions using a block-localized wave function approach. *J. Chem. Phys.* **2000**, *112*, 5530–5538.

(24) Mo, Y.; Song, L.; Lin, Y. Block-localized wavefunction (BLW) method at the density functional theory (DFT) level. *J. Phys. Chem. A* **2007**, *111*, 8291–8301.

(25) Mo, Y.; Bao, P.; Gao, J. Energy decomposition analysis based on a block-localized wavefunction and multistate density functional theory. *Phys. Chem. Chem. Phys.* **2011**, *13*, 6760–6775.

(26) Khaliullin, R. Z.; Cobar, E. A.; Lochan, R. C.; Bell, A. T.; Head-Gordon, M. Unravelling the Origin of Intermolecular Interactions Using Absolutely Localized Molecular Orbitals. *J. Phys. Chem. A* **2007**, *111*, 8753–8765.

(27) Horn, P. R.; Sundstrom, E. J.; Baker, T. A.; Head-Gordon, M. Unrestricted absolutely localized molecular orbitals for energy decomposition analysis: Theory and applications to intermolecular interactions involving radicals. *J. Chem. Phys.* **2013**, *138*, 134119.

(28) Horn, P. R.; Mao, Y.; Head-Gordon, M. Probing non-covalent interactions with a second generation energy decomposition analysis using absolutely localized molecular orbitals. *Phys. Chem. Chem. Phys.* **2016**, *18*, 23067–23079.

(29) Horn, P. R.; Mao, Y.; Head-Gordon, M. Defining the contributions of permanent electrostatics, Pauli repulsion, and dispersion in density functional theory calculations of intermolecular interaction energies. *J. Chem. Phys.* **2016**, *144*, 114107.

(30) Horn, P. R.; Head-Gordon, M. Polarization contributions to intermolecular interactions revisited with fragment electric-field response functions. *J. Chem. Phys.* **2015**, *143*, 114111.

(31) Mao, Y.; Horn, P. R.; Head-Gordon, M. Energy decomposition analysis in an adiabatic picture. *Phys. Chem. Chem. Phys.* **2017**, *19*, 5944–5958.

(32) Ge, Q.; Mao, Y.; Head-Gordon, M. Energy decomposition analysis for exciplexes using absolutely localized molecular orbitals. *J. Chem. Phys.* **2018**, *148*, 064105.

(33) Ge, Q.; Head-Gordon, M. Energy Decomposition Analysis for Excimers Using Absolutely Localized Molecular Orbitals within Time-Dependent Density Functional Theory and Configuration Interaction with Single Excitations. *J. Chem. Theory Comput.* **2018**, *14*, 5156–5168.

(34) Gonthier, J. F.; Thirman, J.; Head-Gordon, M. Understanding Non-Covalent Interactions: Correlated Energy Decomposition Analysis and Applications to Halogen Bonding. *Chimia* **2018**, *72*, 193–198.

(35) Yoo, S.; Aprà, E.; Zeng, X. C.; Xantheas, S. S. High-Level Ab Initio Electronic Structure Calculations of Water Clusters $(H_2O)_{16}$ and $(H_2O)_{17}$: A New Global Minimum for $(H_2O)_{16}$. *J. Phys. Chem. Lett.* **2010**, *1*, 3122–3127.

(36) Mardirossian, N.; Lambrecht, D. S.; McCaslin, L.; Xantheas, S. S.; Head-Gordon, M. The Performance of Density Functionals for Sulfate-Water Clusters. *J. Chem. Theory Comput.* **2013**, *9*, 1368–1380.

(37) Feyereisen, M.; Fitzgerald, G.; Komornicki, A. Use of approximate integrals in ab initio theory. An application in MP2 energy calculations. *Chem. Phys. Lett.* **1993**, *208*, 359–363.

(38) Bernholdt, D. E.; Harrison, R. J. Large-scale correlated electronic structure calculations: the RI-MP2 method on parallel computers. *Chem. Phys. Lett.* **1996**, *250*, 477–484.

(39) Tentscher, P. R.; Arey, J. S. Binding in Radical-Solvent Binary Complexes: Benchmark Energies and Performance of Approximate Methods. *J. Chem. Theory Comput.* **2013**, *9*, 1568–1579.

(40) Su, P.; Li, H. Energy decomposition analysis of covalent bonds and intermolecular interactions. *J. Chem. Phys.* **2009**, *131*, 014102.

(41) Thirman, J.; Head-Gordon, M. Electrostatic Domination of the Effect of Electron Correlation in Intermolecular Interactions. *J. Phys. Chem. Lett.* **2014**, *5*, 1380.

(42) Thirman, J.; Head-Gordon, M. An energy decomposition analysis for second-order Møller–Plesset perturbation theory based on absolutely localized molecular orbitals. *J. Chem. Phys.* **2015**, *143*, 084124.

(43) Schütz, M.; Rauhut, G.; Werner, H.-J. Local treatment of electron correlation in molecular clusters: Structures and stabilities of $(H_2O)_n$, $n = 2 - 4$. *J. Phys. Chem. A* **1998**, *102*, 5997–6003.

(44) Sherrill, C. D.; Takatani, T.; Hohenstein, E. G. An Assessment of Theoretical Methods for Nonbonded Interactions: Comparison to Complete Basis Set Limit Coupled-Cluster Potential Energy Curves for the Benzene Dimer, the Methane Dimer, Benzene–Methane, and Benzene–H2S. *J. Phys. Chem. A* **2009**, *113*, 10146–10159.

(45) Jurečka, P.; Šponer, J.; Černý, J.; Hobza, P. Benchmark database of accurate (MP2 and CCSD(T) complete basis set limit) interaction energies of small model complexes, DNA base pairs, and amino acid pairs. *Phys. Chem. Chem. Phys.* **2006**, *8*, 1985–1993.

(46) Janowski, T.; Ford, A. R.; Pulay, P. Accurate correlated calculation of the intermolecular potential surface in the coronene dimer. *Mol. Phys.* **2010**, *108*, 249–257.

(47) Tkatchenko, A.; DiStasio, R. A.; Head-Gordon, M.; Scheffler, M. Dispersion-corrected Møller–Plesset second-order perturbation theory. *J. Chem. Phys.* **2009**, *131*, 094106.

(48) Schneider, W. B.; Bistoni, G.; Sparta, M.; Saitow, M.; Riplinger, C.; Auer, A. A.; Neese, F. Decomposition of Intermolecular Interaction Energies within the Local Pair Natural Orbital Coupled Cluster Framework. *J. Chem. Theory Comput.* **2016**, *12*, 4778–4792.

(49) Altun, A.; Saitow, M.; Neese, F.; Bistoni, G. Local Energy Decomposition of Open-Shell Molecular Systems in the Domain-Based Local Pair Natural Orbital Coupled Cluster Framework. *J. Chem. Theory Comput.* **2019**, *15*, 1616–1632.

(50) Altun, A.; Neese, F.; Bistoni, G. Effect of Electron Correlation on Intermolecular Interactions: A Pair Natural Orbitals Coupled Cluster Based Local Energy Decomposition Study. *J. Chem. Theory Comput.* **2018**, *15*, 215–228.

(51) Bistoni, G. Finding chemical concepts in the Hilbert space: Coupled cluster analyses of noncovalent interactions. *Wiley Interdiscip. Rev. Comput. Mol. Sci.* **2019**, e1442.

(52) Parker, T. M.; Burns, L. A.; Parrish, R. M.; Ryno, A. G.; Sherrill, C. D. Levels of symmetry adapted perturbation theory (SAPT). I. Efficiency and performance for interaction energies. *J. Chem. Phys.* **2014**, *140*, 094106.

(53) Jeziorski, B.; Moszynski, R.; Szalewicz, K. Perturbation Theory Approach to Intermolecular Potential Energy Surfaces of van der Waals Complexes. *Chem. Rev.* **1994**, *94*, 1887–1930.

(54) Szalewicz, K. Symmetry-adapted perturbation theory of intermolecular forces. *Wiley Interdiscip. Rev. Comput. Mol. Sci.* **2012**, *2*, 254–272.

(55) Hohenstein, E. G.; Jaeger, H. M.; Carrell, E. J.; Tschumper, G. S.; Sherrill, C. D. Accurate Interaction Energies for Problematic Dispersion-Bound Complexes: Homogeneous Dimers of NCCN, P_2, and PCCP. *J. Chem. Theory Comput.* **2011**, *7*, 2842–2851.

(56) Parrish, R. M.; Hohenstein, E. G.; Sherrill, C. D. Tractability gains in symmetry-adapted perturbation theory including coupled double excitations: CCD+ST(CCD) dispersion with natural orbital truncations. *J. Chem. Phys.* **2013**, *139*, 174102.

(57) Thirman, J.; Head-Gordon, M. Efficient Implementation of Energy Decomposition

Analysis for Second-Order Møller–Plesset Perturbation Theory and Application to Anion Interactions. *J. Phys. Chem. A* **2017**, *121*, 717–728.

(58) Lee, M. S.; Maslen, P. E.; Head-Gordon, M. Closely approximating second-order Møller–Plesset perturbation theory with a local triatomics in molecules model. *J. Chem. Phys.* **2000**, *112*, 3592–3601.

(59) DiStasio, R. A.; Jung, Y.; Head-Gordon, M. A Resolution-Of-The-Identity Implementation of the Local Triatomics-In-Molecules Model for Second-Order Møller–Plesset Perturbation Theory with Application to Alanine Tetrapeptide Conformational Energies. *J. Chem. Theory Comput.* **2005**, *1*, 862–876.

(60) Azar, R. J.; Head-Gordon, M. An energy decomposition analysis for intermolecular interactions from an absolutely localized molecular orbital reference at the coupled-cluster singles and doubles level. *J. Chem. Phys.* **2012**, *136*, 024103.

(61) Steinmann, S. N.; Corminboeuf, C. Exploring the Limits of Density Functional Approximations for Interaction Energies of Molecular Precursors to Organic Electronics. *J. Chem. Theory Comput.* **2012**, *8*, 4305–4316.

(62) Mason, K. A.; Pearcy, A. C.; Attah, I. K.; Platt, S. P.; Aziz, S. G.; El-Shall, M. S. Gas phase hydration of halogenated benzene cations. Is it hydrogen or halogen bonding? *Phys. Chem. Chem. Phys.* **2017**, *19*, 18603–18611.

(63) Kamrath, M. Z.; Relph, R. A.; Johnson, M. A. Vibrational Predissociation Spectrum of the Carbamate Radical Anion, $C_5H_5N\text{-}CO_2^-$, Generated by Reaction of Pyridine with $(CO_2)_m^-$. *J. Am. Chem. Soc.* **2010**, *132*, 15508–15511.

(64) Craig, S. M.; Johnson, C. J.; Ranasinghe, D. S.; Perera, A.; Bartlett, R. J.; Berman, M. R.; Johnson, M. A. Vibrational Characterization of Radical Ion Adducts between Imidazole and CO_2. *J. Phys. Chem. A* **2018**, *122*, 3805–3810.

(65) Hylleraas, E. A. Über den Grundterm der Zweielektronenprobleme von H^-, He, Li^+, Be^{++} usw. *Z. Phys.* **1930**, *65*, 209–225.

(66) Neese, F.; Schwabe, T.; Kossmann, S.; Schirmer, B.; Grimme, S. Assessment of Orbital-Optimized, Spin-Component Scaled Second-Order Many-Body Perturbation Theory for Thermochemistry and Kinetics. *J. Chem. Theory Comput.* **2009**, *5*, 3060–3073.

(67) Lee, J.; Head-Gordon, M. Regularized Orbital-Optimized Second-Order Møller–Plesset Perturbation Theory: A Reliable Fifth-Order-Scaling Electron Correlation Model with Orbital Energy Dependent Regularizers. *J. Chem. Theory Comput.* **2018**, *14*, 5203–5219.

(68) Amos, R. D.; Andrews, J. S.; Handy, N. C.; Knowles, P. J. Open-shell Møller–Plesset perturbation theory. *Chem. Phys. Lett.* **1991**, *185*, 256 – 264.

(69) Murray, C.; Davidson, E. R. Perturbation theory for open shell systems. *Chem. Phys. Lett.* **1991**, *187*, 451 – 454.

(70) Hubač, I.; Čársky, P. Correlation energy of open-shell systems. Application of the many-body Rayleigh-Schrödinger perturbation theory in the restricted Roothaan-Hartree-Fock formalism. *Phys. Rev. A* **1980**, *22*, 2392–2399.

(71) Lee, T. J.; Jayatilaka, D. An open-shell restricted Hartree-Fock perturbation theory based on symmetric spin orbitals. *Chem. Phys. Lett.* **1993**, *201*, 1 – 10.

(72) Knowles, P. J.; Andrews, J. S.; Amos, R. D.; Handy, N. C.; Pople, J. A. Restricted Møller–Plesset theory for open-shell molecules. *Chem. Phys. Lett.* **1991**, *186*, 130 – 136.

(73) Lauderdale, W. J.; Stanton, J. F.; Gauss, J.; Watts, J. D.; Bartlett, R. J. Many-body

perturbation theory with a restricted open-shell Hartree-Fock reference. *Chem. Phys. Lett.* **1991**, *187*, 21 – 28.

(74) Nagata, T.; Takahashi, O.; Saito, K.; Iwata, S. Basis set superposition error free self-consistent field method for molecular interaction in multi-component systems: Projection operator formalism. *J. Chem. Phys.* **2001**, *115*, 3553–3560.

(75) Löwdin, P.-O. On the non-orthogonality problem connected with the use of atomic wave functions in the theory of molecules and crystals. *J. Chem. Phys.* **1950**, *18*, 365–375.

(76) Handy, N. C.; Schaefer, H. F. On the evaluation of analytic energy derivatives for correlated wave functions. *J. Chem. Phys.* **1984**, *81*, 5031–5033.

(77) Seeger, R.; Pople, J. A. Self-consistent molecular orbital methods. XVIII. Constraints and stability in Hartree-Fock theory. *J. Chem. Phys.* **1977**, *66*, 3045–3050.

(78) Tozer, D. J.; Andrews, J. S.; Amos, R. D.; Handy, N. C. Gradient theory applied to restricted (open-shell) Møller–Plesset theory. *Chem. Phys. Lett.* **1992**, *199*, 229 – 236.

(79) Rhee, Y. M.; DiStasio, R. A.; Lochan, R. C.; Head-Gordon, M. Analytical gradient of restricted second-order Møller–Plesset correlation energy with the resolution of the identity approximation, applied to the TCNE dimer anion complex. *Chem. Phys. Lett.* **2006**, *426*, 197 – 203.

(80) Boys, S.; Bernardi, F. The calculation of small molecular interactions by the differences of separate total energies. Some procedures with reduced errors. *Mol. Phys.* **1970**, *19*, 553–566.

(81) Chai, J.-D.; Head-Gordon, M. Long-range corrected hybrid density functionals with damped atom-atom dispersion corrections. *Phys. Chem. Chem. Phys.* **2008**, *10*, 6615–6620.

(82) Weigend, F.; Ahlrichs, R. Balanced basis sets of split valence, triple zeta valence and quadruple zeta valence quality for H to Rn: Design and assessment of accuracy. *Phys. Chem. Chem. Phys.* **2005**, *7*, 3297–3305.

(83) Rappoport, D.; Furche, F. Property-optimized Gaussian basis sets for molecular response calculations. *J. Chem. Phys.* **2010**, *133*, 134105.

(84) Peterson, K. A.; Figgen, D.; Goll, E.; Stoll, H.; Dolg, M. Systematically convergent basis sets with relativistic pseudopotentials. II. Small-core pseudopotentials and correlation consistent basis sets for the post-d group 16–18 elements. *J. Chem. Phys.* **2003**, *119*, 11113–11123.

(85) Dunning, T. H. Gaussian basis sets for use in correlated molecular calculations. I. The atoms boron through neon and hydrogen. *J. Chem. Phys.* **1989**, *90*, 1007–1023.

(86) Kendall, R. A.; Dunning, T. H.; Harrison, R. J. Electron affinities of the row atoms revisited. Systematic basis sets and wave functions. *J. Chem. Phys.* **1992**, *96*, 6796–6806.

(87) Woon, D. E.; Dunning, T. H. Gaussian basis sets for use in correlated molecular calculations. III. The atoms aluminum through argon. *J. Chem. Phys.* **1993**, *98*, 1358–1371.

(88) Weigend, F.; Köhn, A.; Hättig, C. Efficient use of the correlation consistent basis sets in resolution of the identity MP2 calculations. *J. Chem. Phys.* **2002**, *116*, 3175–3183.

(89) Hättig, C. Optimization of auxiliary basis sets for RI-MP2 and RI-CC2 calculations: Corevalence and quintuple- basis sets for H to Ar and QZVPP basis sets for Li to Kr. *Phys. Chem. Chem. Phys.* **2005**, *7*, 59–66.

(90) Mardirossian, N.; Head-Gordon, M. Survival of the most transferable at the top of

Jacob's ladder: Defining and testing the ωB97M(2) double hybrid density functional. *J. Chem. Phys.* **2018**, *148*, 241736.

(91) Hellweg, A.; Rappoport, D. Development of new auxiliary basis functions of the Karlsruhe segmented contracted basis sets including diffuse basis functions (def2-SVPD, def2-TZVPPD, and def2-QVPPD) for RI-MP2 and RI-CC calculations. *Phys. Chem. Chem. Phys.* **2015**, *17*, 1010–1017.

(92) Khaliullin, R. Z.; Bell, A. T.; Head-Gordon, M. Analysis of charge transfer effects in molecular complexes based on absolutely localized molecular orbitals. *J. Chem. Phys.* **2008**, *128*, 184112.

(93) Mardirossian, N.; Head-Gordon, M. wB97M-V: A combinatorially optimized, range-separated hybrid, meta-GGA density functional with VV10 nonlocal correlation. *J. Chem. Phys.* **2016**, *144*, 214110.

(94) Mardirossian, N.; Head-Gordon, M. Thirty years of density functional theory in computational chemistry: an overview and extensive assessment of 200 density functionals. *Mol. Phys.* **2017**, *115*, 2315–2372.

(95) Manna, D.; Kesharwani, M. K.; Sylvetsky, N.; Martin, J. M. Conventional and explicitly correlated ab initio benchmark study on water clusters: Revision of the BEGDB and WATER27 data sets. *J. Chem. Theory Comput.* **2017**, *13*, 3136–3152.

(96) Shao, Y.; Gan, Z.; Epifanovsky, E.; Gilbert, A. T.; Wormit, M.; Kussmann, J.; Lange, A. W.; Behn, A.; Deng, J.; Feng, X. et al. Advances in molecular quantum chemistry contained in the Q-Chem 4 program package. *Mol. Phys.* **2015**, *113*, 184–215.

(97) Gilbert, A. T. B.; Besley, N. A.; Gill, P. M. W. Self-Consistent Field Calculations of Excited States Using the Maximum Overlap Method (MOM). *J. Phys. Chem. A* **2008**, *112*, 13164–13171.

(98) Levine, D. S.; Horn, P. R.; Mao, Y.; Head-Gordon, M. Variational Energy Decomposition Analysis of Chemical Bonding. 1. Spin-Pure Analysis of Single Bonds. *J. Chem. Theory Comput.* **2016**, *12*, 4812–4820.

(99) Levine, D. S.; Head-Gordon, M. Energy decomposition analysis of single bonds within Kohn–Sham density functional theory. *Proc. Natl. Acad. Sci. U.S.A* **2017**, *114*, 12649–12656.

(100) Polo, V.; Kraka, E.; Cremer, D. Electron correlation and the self-interaction error of density functional theory. *Mol. Phys.* **2002**, *100*, 1771–1790.

(101) Lundberg, M.; Siegbahn, P. E. M. Quantifying the effects of the self-interaction error in DFT: When do the delocalized states appear? *J. Chem. Phys.* **2005**, *122*, 224103.

(102) Tentscher, P. R.; Arey, J. S. On the nature of interactions of radicals with polar molecules. *J. Phys. Chem. A* **2013**, *117*, 12560–12568.

(103) Ramos-Cordoba, E.; Lambrecht, D. S.; Head-Gordon, M. Charge-transfer and the hydrogen bond: Spectroscopic and structural implications from electronic structure calculations. *Faraday Discuss.* **2011**, *150*, 345–362.

(104) Khaliullin, R. Z.; Bell, A. T.; Head-Gordon, M. Electron donation in the water–water hydrogen bond. *Chem.-Eur. J.* **2009**, *15*, 851–855.

(105) Meot-Ner, M. The Ionic Hydrogen Bond. *Chem. Rev.* **2005**, *105*, 213–284.

(106) R., D. G.; Shing, H. P.; Lars, K.; C., L. A.; Roberto, M.; Pierangelo, M.; Peter, P.; Giuseppe, R.; Kari, R. *Pure Appl. Chem.* **2013**, *85*, 1711–1713.

(107) Clark, T.; Hennemann, M.; Murray, J. S.; Politzer, P. Halogen bonding: the σ-hole. *J. Mol. Model.* **2007**, *13*, 291–296.

(108) Clark, T.; Heßelmann, A. The coulombic σ-hole model describes bonding in $CX_3I\cdots Y^-$ complexes completely. *Phys. Chem. Chem. Phys.* **2018**, *20*, 22849–22855.

(109) Huber, S. M.; Jimenez-Izal, E.; Ugalde, J. M.; Infante, I. Unexpected trends in halogen-bond based noncovalent adducts. *ChemComm* **2012**, *48*, 7708–7710.

(110) Grabowski, S. J. Hydrogen and halogen bonds are ruled by the same mechanisms. *Phys. Chem. Chem. Phys.* **2013**, *15*, 7249–7259.

(111) Wang, C.; Danovich, D.; Mo, Y.; Shaik, S. On The Nature of the Halogen Bond. *J. Chem. Theory Comput.* **2014**, *10*, 3726–3737.

(112) Thirman, J.; Engelage, E.; Huber, S. M.; Head-Gordon, M. Characterizing the interplay of Pauli repulsion, electrostatics, dispersion and charge transfer in halogen bonding with energy decomposition analysis. *Phys. Chem. Chem. Phys.* **2018**, *20*, 905–915.

(113) Angarov, V.; Kozuch, S. On the σ, π and δ Hole Interactions: a Molecular Orbital Overview. *New J. Chem* **2018**, *42*, 1413–1422.

(114) Ang, S. J.; Mak, A. M.; Wong, M. W. Nature of halogen bonding involving systems, nitroxide radicals and carbenes: a highlight of the importance of charge transfer. *Phys. Chem. Chem. Phys.* **2018**, *20*, 26463–26478.

(115) Řezáč, J.; de la Lande, A. On the role of charge transfer in halogen bonding. *Phys. Chem. Chem. Phys.* **2017**, *19*, 791–803.

(116) Nepal, B.; Scheiner, S. NX$\cdots$Y halogen bonds. Comparison with NH$\cdots$Y H-bonds and CX$\cdots$Y halogen bonds. *Phys. Chem. Chem. Phys.* **2016**, *18*, 18015–18023.

(117) Benz, S.; Poblador-Bahamonde, A. I.; Low-Ders, N.; Matile, S. Catalysis with Pnictogen, Chalcogen, and Halogen Bonds. *Angew. Chem. Int. Ed.* **2018**, *130*, 5506–5510.

(118) Concepcion, J. J.; House, R. L.; Papanikolas, J. M.; Meyer, T. J. Chemical approaches to artificial photosynthesis. *Proc. Natl. Acad. Sci. U.S.A.* **2012**, *109*, 15560–15564.

(119) Alstrum-Acevedo, J. H.; Brennaman, M. K.; Meyer, T. J. Chemical Approaches to Artificial Photosynthesis. 2. *Inorg. Chem.* **2005**, *44*, 6802–6827.

(120) Barton, E. E.; Rampulla, D. M.; Bocarsly, A. B. Selective Solar-Driven Reduction of CO_2 to Methanol Using a Catalyzed *p*-GaP Based Photoelectrochemical Cell. *J. Am. Chem. Soc.* **2008**, *130*, 6342–6344.

(121) Bocarsly, A. B.; Gibson, Q. D.; Morris, A. J.; L'Esperance, R. P.; Detweiler, Z. M.; Lakkaraju, P. S.; Zeitler, E. L.; Shaw, T. W. Comparative Study of Imidazole and Pyridine Catalyzed Reduction of Carbon Dioxide at Illuminated Iron Pyrite Electrodes. *ACS Catal.* **2012**, *2*, 1684–1692.

(122) DeLuca, M. J.; Niu, B.; Johnson, M. A. Photoelectron spectroscopy of $(CO_2)_n^-$ clusters with $2 \leq n \leq 13$: Cluster size dependence of the core molecular ion. *J. Chem. Phys.* **1988**, *88*, 5857–5863.

(123) Shin, J.-W.; Hammer, N. I.; Johnson, M. A.; Schneider, H.; Glöß, A.; Weber, J. M. An Infrared Investigation of the $(CO_2)_n^-$ Clusters: Core Ion Switching from Both the Ion and Solvent Perspectives. *J. Phys. Chem. A* **2005**, *109*, 3146–3152.

(124) Thompson, M. C.; Weber, J. M. Enhancement of infrared activity by moving electrons through bonds — The case of CO_2 anion and carboxylate. *Chem. Phys. Lett.* **2017**, *683*, 586–590.

(125) Han, S. Y.; Chu, I.; Kim, J. H.; Song, J. K.; Kim, S. K. Photoelectron spectroscopy and ab initio study of mixed cluster anions of $[(CO_2)_{1-3}(\text{Pyridine})_{1-6}]^-$: Formation of a covalently bonded anion core of $(C_5H_5N^-CO_2)^-$. *J. Chem. Phys.* **2000**, *113*, 596–601.

(126) Lee, J.; Head-Gordon, M. Distinguishing artificial and essential symmetry breaking in a single determinant: approach and application to the C_{60}, C_{36}, and C_{20} fullerenes. *Phys. Chem. Chem. Phys.* **2019**, *21*, 4763–4778.

(127) Lee, J.; Head-Gordon, M. Two single-reference approaches to singlet biradicaloid problems: Complex, restricted orbitals and approximate spin-projection combined with regularized orbital-optimized Møller–Plesset perturbation theory. *J. Chem. Phys.* **2019**, *150*, 244106.

(128) Goerigk, L.; Grimme, S. Double-hybrid density functionals. *WIREs Comput. Mol. Sci.* **2014**, *4*, 576–600.

(129) Bertels, L. W.; Lee, J.; Head-Gordon, M. Third-Order Møller–Plesset Perturbation Theory Made Useful? Choice of Orbitals and Scaling Greatly Improves Accuracy for Thermochemistry, Kinetics and Intermolecular Interactions. *J. Phys. Chem. Lett.* **2019**, *10*, 4170–4176.

Graphical TOC Entry